

## Regular Article

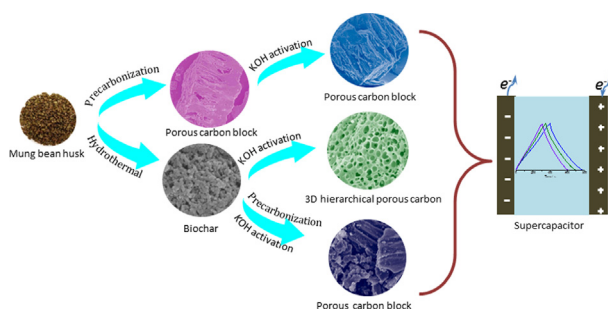
# Biowaste-based porous carbon for supercapacitor: The influence of preparation processes on structure and performance



Mingyuan Song, Yuhao Zhou, Xue Ren, Jiafeng Wan<sup>\*</sup>, Yueyao Du, Guang Wu, Fangwei Ma<sup>\*</sup>

Key Laboratory of Functional Inorganic Material Chemistry, Ministry of Education of China, Key Laboratory of Chemical Engineering Processes & Technology for High-efficiency Conversion (College of Heilongjiang Province), School of Chemistry and Material Science, Heilongjiang University, Harbin 150080, China

## GRAPHICAL ABSTRACT



## ARTICLE INFO

## Article history:

Received 20 July 2018

Revised 10 September 2018

Accepted 17 September 2018

Available online 24 September 2018

## Keywords:

Biowastes

Porous carbon

Supercapacitor

Hierarchical porous structure

## ABSTRACT

Here, a series of porous carbon based supercapacitor electrode materials have been synthesized by means of pyrolysis and hydrothermal methods combining with KOH activation using the biomass wastes mung bean husks as resources. The influence of synthesis process on the morphology, structure and supercapacitor performance of mung bean husks derived porous carbons has been investigated systematically. Especially, it is found that these oxygen-containing groups on the biochar play a crucial role in fabricating the three-dimensional (3D) hierarchical porous structure carbon. The original bio-structured porous carbon (PC<sub>3-600</sub>), the 3D architecture porous carbon (HPC<sub>2-700</sub>) and the porous carbon block (HPPC<sub>2-700</sub>) have a high specific surface area, and the former mainly contains micropores and the latter two possess multistage pores. The specific capacitance of PC<sub>3-600</sub>, HPC<sub>2-700</sub> and HPPC<sub>2-700</sub> is respectively up to 390 F g<sup>-1</sup>, 353 F g<sup>-1</sup>, 304 F g<sup>-1</sup> at 1 A g<sup>-1</sup>, and still maintains as high as 287 F g<sup>-1</sup>, 270 F g<sup>-1</sup> and 235 F g<sup>-1</sup> with corresponding retention ratio of 73.5%, 76.48%, 77.3% even at a high current density of 50 A g<sup>-1</sup>. HPC<sub>2-700</sub>//HPC<sub>2-700</sub> symmetric supercapacitor achieves a high energy density of 20.4 Wh kg<sup>-1</sup> at 872 W kg<sup>-1</sup> in 1 M Na<sub>2</sub>SO<sub>4</sub> electrolyte.

© 2018 Elsevier Inc. All rights reserved.

## 1. Introduction

With the popularity of portable electronic devices and the increasing environmental problems, there has been a surge in

demand on new types of efficient, smaller and more flexible energy storage devices [1,2]. The new generation of energy storage system not only needs to meet the sustainable development, but also needs to have higher power density, longer cycle life and friendly operating environment. Supercapacitor, as an advanced energy storage system, can cater to the above requirements. Therefore, supercapacitor has recently drawn much attention and has a broader range of application [3–5].

<sup>\*</sup> Corresponding authors.

E-mail addresses: [wanjiafeng@hlju.edu.cn](mailto:wanjiafeng@hlju.edu.cn) (J. Wan), [fangwei\\_ma@hotmail.com](mailto:fangwei_ma@hotmail.com) (F. Ma).

According to its energy storage mechanism, supercapacitor can divide into electrochemical double layer capacitors (EDLCs) and pseudocapacitors. Although pseudocapacitor usually has a larger specific capacitance, which is produced based on redox reaction occurring on the surface of the metal oxide electrode [6]. However, these electrode materials generally have some obvious disadvantages, such as poor cycle stability, unsatisfactory electrical conductivity, and high price, which greatly limit their practical application. On the contrary, the EDLCs store energy originating from an electric double layer capacitance formed between the electrode/electrolyte, this endows it excellent stability and good rate performance. The key part of the EDLCs is the electrode, so the exploration of the advanced electrode materials with high specific surface area is very important for improving the performance of the EDLCs [7].

Porous carbon has been widely used and is the most promising electrode material for EDLCs. Porous carbon materials have many advantages, such as relatively inexpensive, easy to gain and environment-friendly [8]. Especially these carbon materials with well-developed pore structure, high specific surface area, and good electrical conductivity are satisfactory for the application of in supercapacitor. These porous carbons could be prepared by hard template method [9], soft template method [10], pyrolysis combined with activation method [11–15], hydrothermal method [16], molten-salt synthesis [17], and so on. On the one hand, preparing process is an important factor in the construction of porous carbon materials. On the other hand, raw materials are also the decisive factors that affect the structural properties of porous carbon materials. Currently, many kinds of carbon precursors have been studied, such as biomass [18], coal-based [19], petroleum [20] and the like. Among them, biomass wastes have attracted great attention due to their advantages of being renewable, environmentally friendly and widely sourced, such as dead leaves of ficus religiosa [21], corn cob [22], kenaf stem [23], sunflower heads [24]. It is estimated that biomass wastes account for about 10% of the global energy reserves [25]. Annual biological production will be up to  $1.08 \times 10^{11}$  tons (tons of oil equivalent), equivalent to 10 times of the global energy demand [26]. In many developing countries, waste biomass is mainly disposed of by landfill or directly incinerated, which have caused serious environmental pollution and the waste of resources. It is of great significance and value to transform these wastes into high value-added chemical products through appropriate process treatment. In order to make full use of resources and develop a sustainable chemistry, the adoption of a simple process to convert waste biomass into high value-added, high-performance porous carbon materials is very promising.

Mung beans are widely grown in most parts of the world (tropical and subtropical). In China, the total output of mung beans in 2016 reached 610,000 tons. Among various organs of mung bean, mung bean husk accounts for 7–10% of the total mass of mung bean [27]. Generally, during the processing of the mung bean, such as producing mung bean powder and mung bean sprout, most of mung bean husks are discarded and only a few is applied to feeds, due to its poor taste and high hardness. This caused a serious waste of resources and increased the pressure of waste disposal. At present, much attention has been paid to the treatment of mung bean husks, such as extracting dietary fiber and other nutrients from mung bean husks [28–30]. As far as we know, there is no report on mung bean husks-based porous carbon up to now. It is very valuable to explore the preparation processing of mung bean husks-based porous carbon for increasing their additional value and effective utilization of waste resource.

It is well known that direct carbonization is the best method for maintaining the original carbon skeleton morphology of biomass [31,32]. In addition, the hydrothermal method is a unique and

efficient method for preparing biochar. The hydrothermal process can hydrolyze the lignin and hemicellulose in the biomass and reduce the crystallinity of the cellulose to increase the porosity of the biomass; this may increase the proportion of mesopores in biochar [33]. Not only those, the hydrothermal process can also increase the oxygen content of biochar, contributing to improve the wettability and provides pseudo-capacitance [34]. Therefore, we intend to use the above two methods to prepare high-performance mung bean husk-based porous carbon, and to explore the influence of the preparation process on the morphology, structure and performance of carbon materials.

In this work, low-cost biowaste mung bean husks were utilized as a sustainable carbon source to prepare add-valued porous carbon materials. First, PC<sub>3-600</sub> (pyrolysis-carbon) was prepared by pre-carbonizing mung bean husk followed by KOH activation. The PC<sub>3-600</sub> sample retains an original biomass structure of mung bean husk and has a high specific surface area of  $2131 \text{ m}^2 \text{ g}^{-1}$ . Second, biochar was prepared by hydrothermal treatment of mung bean husk in  $\text{H}_2\text{SO}_4$  aqueous solution. The HPC<sub>2-700</sub> (hydrothermal-pyrolysis-carbon) with 3D hierarchical porous structure was synthesized through simple KOH activation. The HPC<sub>2-700</sub> has a higher specific surface area ( $1214 \text{ m}^2 \text{ g}^{-1}$ ) and excellent capacitive properties with a high specific capacitance of  $353 \text{ F g}^{-1}$  at  $1 \text{ A g}^{-1}$  and corresponding admirable retention ratio of 76.48% at  $50 \text{ A g}^{-1}$  in a three-electrode system.

## 2. Experimental sections

### 2.1. Materials

Mung bean husk was purchased at a mung bean food processing plant in Harbin. Sulfuric acid (98 wt%), potassium hydroxide (AR, 85.0 wt%), and hydrochloric acid (AR, 36.0 wt%), were purchased from Tianjin Kermel Chemical Reagent Company Limited.

### 2.2. Preparation of the PCs

4 g of mung bean husk was dried at  $40^\circ\text{C}$  and then heat-treated under the protection of nitrogen at  $700^\circ\text{C}$  for 1 h. To remove impurities, the pyrolysis product was mixed with 1 M hydrochloric acid and stirred for 2 h, then washed with distilled water and dried at  $120^\circ\text{C}$ . The obtained sample is named as PC. 0.5 g of PC were mixed with 2 ml KOH ethanol solution of 1.5 g KOH and standing for 6 h, and then the mixture were dried at  $80^\circ\text{C}$ . Thereafter, the sample was underwent pyrolysis under the target temperature of  $600^\circ\text{C}$  for 1 h, the next process of removing impurities is the same as that of the PC. The final prepared activated carbon material is named as PC<sub>3-600</sub>. Where 3 is the mass ratio of KOH and PC, and 600 is the activation temperature.

### 2.3. Preparation of the HPCs and HPPCs

4 g of mung bean husks were mixed with 2 M  $\text{H}_2\text{SO}_4$  and subjected to hydrothermal carbonization at  $180^\circ\text{C}$  for 12 h. Then, the hydrochar was obtained by centrifugal separation and dried at  $120^\circ\text{C}$ . 0.5 g of biochar was mixed with 12 ml ethanol solution with 1.0 g KOH and standing for 6 h and then the mixture were dried at  $80^\circ\text{C}$ . The obtained sample was pyrolyzed at  $700^\circ\text{C}$  for 1 h. After removing impurities, the HPC<sub>2-700</sub> sample was obtained. For comparison, biochar was first heated at  $700^\circ\text{C}$  for 1 h in the  $\text{N}_2$  to obtain HPC. Subsequently, 0.5 g of HPPC was activated with 1.0 g KOH at  $700^\circ\text{C}$  for 1 h to prepare HPPC<sub>2-700</sub>.

## 2.4. Material characterizations

Hitachi S-4800 instrument was used to acquire the Scanning electron microscopy (SEM) micrographs. X-ray diffraction (XRD) was measured by using Rigaku D/max-III B with copper radiation (CuK $\alpha$ , 0.15406 nm). Raman spectra were operated with Jobin Yvon HR 800 micro-Raman spectrometer at 458 nm. The nitrogen adsorption and desorption isotherms were measured at  $-196^\circ\text{C}$  with a Quadachrome AUTOSORB-1-MP Adsorption Instrument. The specific surface area was calculated by Brunauer-Emmett-Teller (BET) method and the pore size distribution was determined by the density functional theory (DFT) using the desorption branch data. The X-ray photoelectron spectroscopy (XPS) was performed on a VG ESCALAB MK II (VGScientific, UK).

## 2.5. Electrochemical measurements

Electrochemical testing was tested with CHI 660E electrochemical workstation (Shanghai Chenhua, China). The electrolytic liquid system is 6 M KOH or 1 M Na $_2$ SO $_4$  solution. Platinum foil ( $1.5 \times 1.5\text{ cm}^2$ ) and Hg/HgO were used as counter and reference electrodes. Acetylene black is used as a conductive agent, poly (tetrafluoroethylene) is used as a binder, and foamed nickel is used as a current collector. The active sample, acetylene black, and poly (tetrafluoroethylene) were mixing uniformly in a mass ratio 80:10:10 to fabricate a working electrode (the active mass is about  $2.0\text{ mg cm}^2$ ). First, the electrochemical performance of the electrode was tested by a three electrode system. The specific gravimetric capacitance was calculated from the discharge process on the basis of:

$$C_s = \frac{I\Delta t}{m\Delta V}$$

where  $I$  (A) is the discharge current,  $\Delta t$  (s) is the discharge time,  $m$  (g) is the mass of active material, and  $\Delta V$  (V) is the potential change after  $IR$  drop during the discharge process.

Second, the electrochemical performance of the samples was tested by a symmetrical electrode system. 6 M KOH solution and 1 M Na $_2$ SO $_4$  solution serve as electrolyte. The specific capacitance for the single electrode was calculated according to:

$$C_s = \frac{4I\Delta t}{m\Delta V}$$

where  $I$  (A),  $\Delta t$  (s),  $m$  (g),  $\Delta V$  (V) are the discharge current, the discharge time, the total mass of active material in both electrodes, and the potential change after  $IR$  drop during the discharge process, respectively. The energy density and power density of symmetrical supercapacitor system were calculated according to:

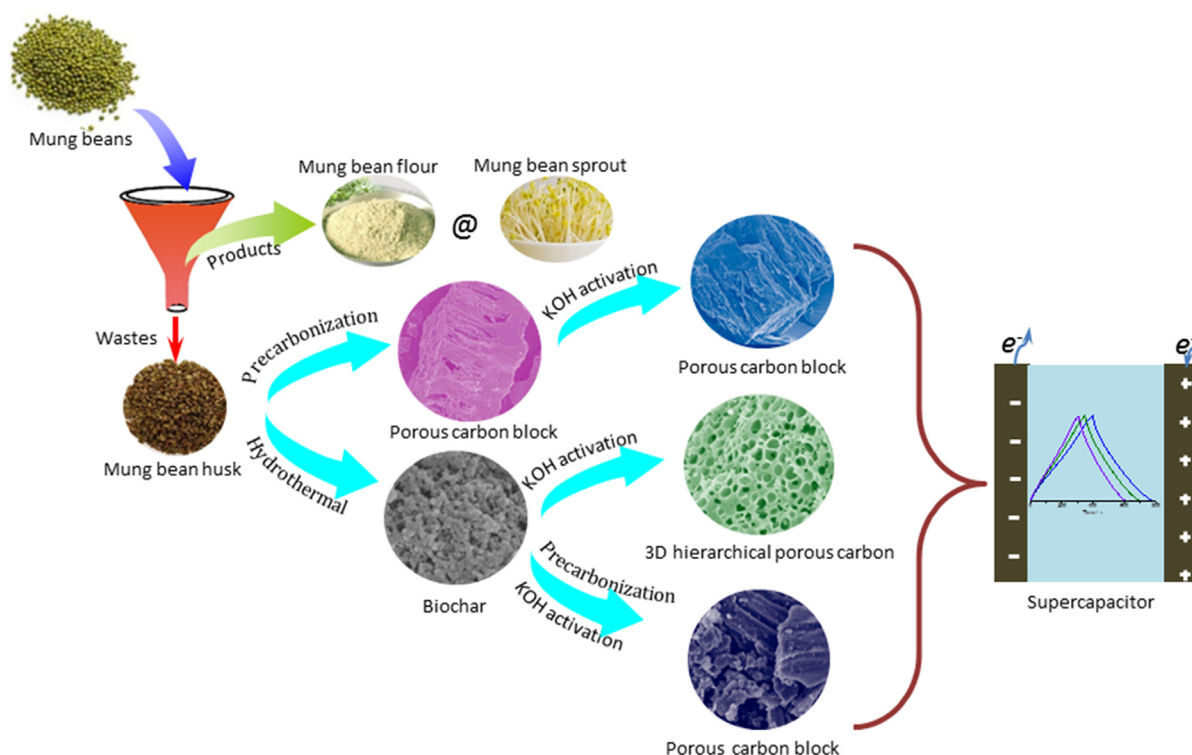
$$E_t = \frac{C_t(\Delta V)^2}{2 \times 3.6}$$

$$P_t = \frac{E_t}{t} \times 3600$$

where  $E_t$  (Wh  $\text{kg}^{-1}$ ) is the specific energy density,  $P_t$  (W  $\text{kg}^{-1}$ ) is the specific power density,  $C_t$  (F  $\text{g}^{-1}$ ) is the specific capacitance of the total symmetrical system,  $\Delta V$  (V) is the cell voltage for charging and discharging excluding the  $IR$  drop during the discharge process, and  $\Delta t$  (s) is the discharge time.

## 3. Results and discussions

**Scheme 1** illustrates the source of mung bean husks and the preparation process of mung bean husks-based porous carbon materials. In the food industry, mung beans are generally processed into green bean sprouts, mung bean flour and other foods. As a byproduct, a large amount of mung bean husks are discarded during the production of these foods due to poor taste. Here, the preparation processes of diverse mung bean husks-based porous carbons have been developed. Firstly, the bulk porous carbon was prepared by pre-carbonization combined with KOH activation. Secondly, mung bean husks were subjected to hydrothermal



**Scheme 1.** Schematic illustration for the preparation of mung bean husk-based porous carbons.

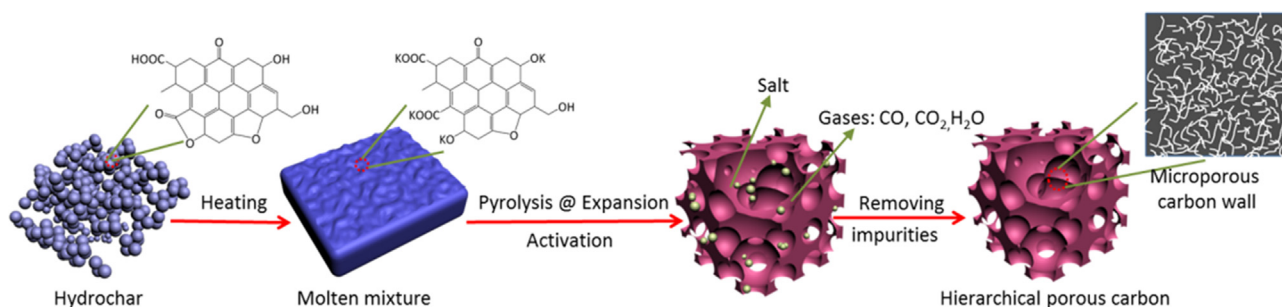


treatment to obtain granular biochar. These biochar were directly activated by KOH to prepare 3D hierarchical porous carbon. In addition, these biochar were also pre-carbonized and then activated to produce porous carbon bulk. These prepared porous carbons were used for the electrode material to investigate their supercapacitor performance (see Scheme 2).

Mung bean husks were first carried out preliminary carbonization and then KOH activation to obtain PC and PC<sub>3-600</sub> with the original biomass structure of mung bean husk. The SEM image (Fig. 1a) of the PCs sample shows the section structure with asymmetric feature. One side is with array shaped macroporous structure like bushes and the other side is with solid structure without macropores. This particular structure is inherited from the biological structure of mung bean husk. The PC<sub>3-600</sub> sample (Fig. 1b) obtained after KOH activation maintains the similar morphology and structure with the PCs. Moreover, many interlinked particles exist in the wide fracture. The TEM image (Fig. 1d) indicates that the PC<sub>3-600</sub> sample contains a large number of worm-like micropores produced by KOH etching, meaning that the sample has a high specific surface area to supply enriched interfaces for storing charge.

The SEM images of HPC<sub>2-700</sub> obtained by KOH activating biochar are shown in Fig. 2a, b. The HPC<sub>2-700</sub> exhibits a typical 3D

honeycomb-like architectures fabricated by interconnected macropores and carbon walls, which is beneficial for fast transport of ions and rapid electron transport to optimize rate performance for supercapacitor [35]. These macropores are open and the size of which ranges from 250 nm to 620 nm. Those carbon walls are with the thickness of ~400 nm, providing a large amount of interface for charge storage. The microscopic structure of biochar is also reflected in Fig. S1a and shows the irregular block morphology. From the high magnification SEM photo (Fig. S1b), it can be seen that the biochar block is consisting of a number of interlinked quasi-spherical nanoparticles with the diameter of about 3.3–8.3 nm. Therefore, the microstructure has changed significantly from irregular block to 3D frame structure through heat-treating with the adding of KOH. When decreasing the KOH ratio, the HPC<sub>1-700</sub> still displays the 3D hierarchical porous structure (Fig. S1c). Compared with the HPC<sub>2-700</sub>, the openness of pore structure in the HPC<sub>1-700</sub> is significantly worsened and the macropore size has reduced to 100–200 nm (Fig. S1d). The TEM images (Fig. 2c, d) further show that the HPC<sub>2-700</sub> has the unique 3D hierarchical porous texture composed of macropores and flake-like carbon walls. The high-magnification TEM image (Fig. 2d) demonstrates a large number of micropores and a small amount of microcrystalline regions existed in the carbon wall, illustrating that the



**Scheme 2.** Schematic diagram of the formation process of the 3D hierarchical porous structure.

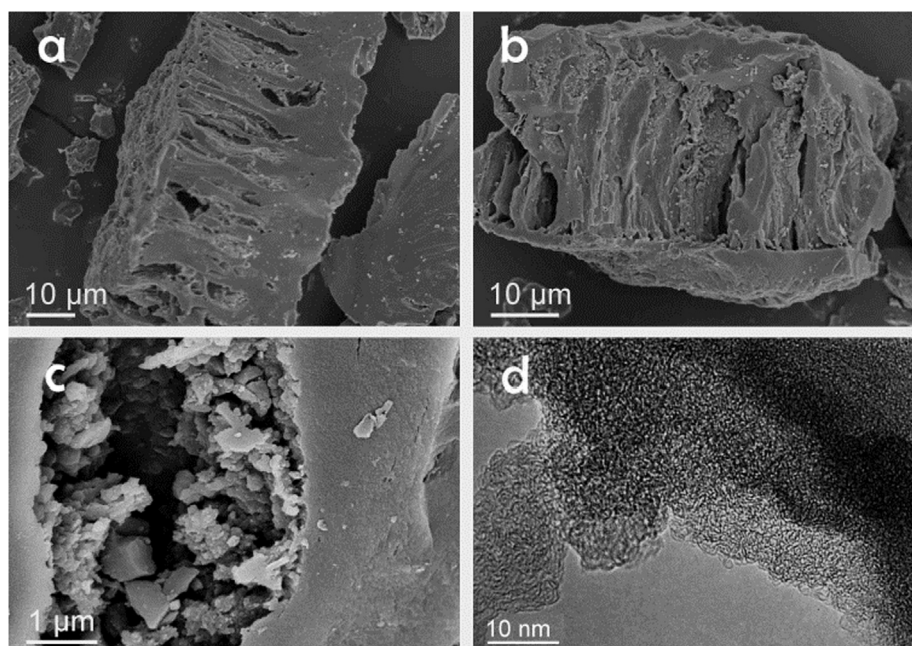


**Fig. 1.** SEM (a) PC, (b) (c) of PC<sub>3-600</sub> and TEM (d) images of images of PC<sub>3-600</sub>.

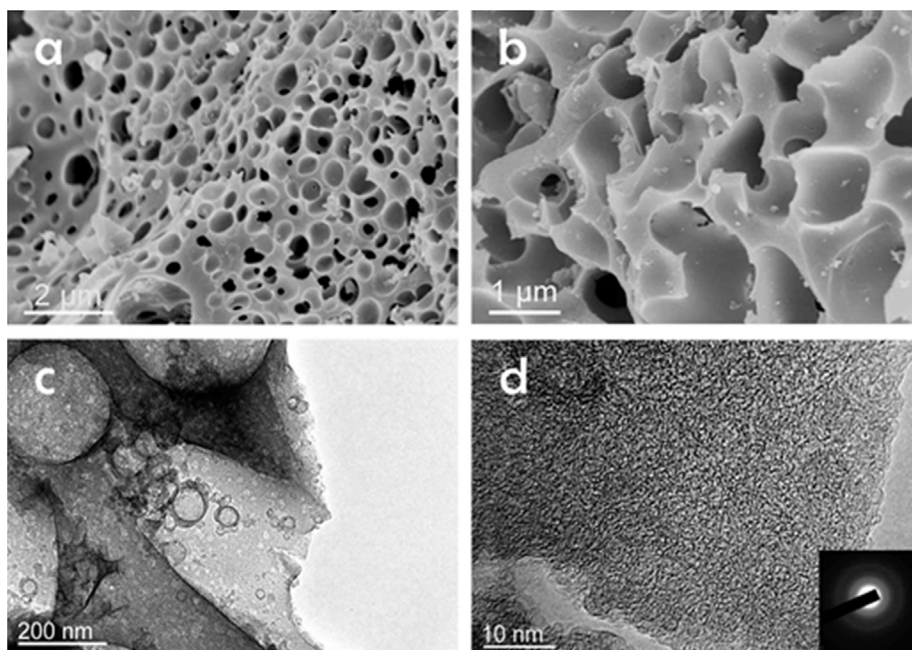


Fig. 2. SEM (a, b) and TEM (c, d) images of HPC<sub>2-700</sub>, the inset in (d) is the corresponding SAED pattern.

material is dominated by amorphous carbon. Besides, an indistinct diffraction ring in the SAED diagram (inset in Fig. 2d) indicates that the sample has a low degree of crystallinity.

In order to study the influence of pre-pyrolyzing biochar on the derived activation carbon, the biochar was pyrolyzed to obtain HPC and then activated by KOH to prepare HPPC<sub>2-700</sub>. The SEM image (Fig. S2a) shows that the HPC maintains the block morphology like biochar. The high magnification SEM photo (Fig. S2b) clearly reveals that the surface structure of HPC is different from that of biochar (Fig. S1b) and the interlinked particles have disappeared, indicating that those biochar particles have recombined and thermal decomposed during the heat-treatment. After KOH activation, the morphology and structure of obtained HPPC<sub>2-700</sub> sample (Fig. 3a, b) has not changed insignificantly still presenting blocky morphology. The structure is completely different from that of the HPC<sub>2-700</sub> prepared by direct activation from biochar (Fig. 2a).

Based on the above results, the pre-pyrolysis of biochar has an important influence on the biochar-derived porous carbon structure. To make clear the formation mechanism of 3D multistage pore structure carbon, some tests and discussion were also carried out. Fig. S3 shows the FT-IR spectra of biochar and HPC. The broad bands at 1100–1450 cm<sup>-1</sup> are attributed to C–O (hydroxyl, lactones, or ether carboxyl) stretching and –OH bending modes. While a band at 1620 cm<sup>-1</sup> was identified as the vibrations of C=C. The bonds at 1705 cm<sup>-1</sup> can be assigned to C=O stretching of carbonyl, quinone, ester, or carboxyl. The bonds at 2855 and

2922 cm<sup>-1</sup> were identified as C–H bond and a wide band at 3430 cm<sup>-1</sup> was identified as the stretching vibrations of –OH [36]. Therefore, the biochar is enriched in oxygen functional groups. However, the intensity of bands for the HPC sample obtained by heat treating at higher temperature are much weaker than those of biochar, suggesting that dehydration and decarbonylation reactions have been taken place during the heat-treating. Thus, it can be speculated that these oxygen-containing groups on the surface of the biochar have played a critical role in the formation of 3D hierarchical porous carbon. The biochar was first mixed with KOH, and KOH would react with these oxygen-containing groups during the heating process to produce corresponding potassium salts and then form a molten mixture of potassium salts and biochar. At higher temperature, these potassium salts and biochar begin to pyrolysis to produce CO, CO<sub>2</sub>, H<sub>2</sub>O and other gases, and meantime the molten mixture could expand like bread leavening that involves the escape of gases to generate a porous structure, similar to soft template [37]. As the gases overflow, the continuous pore structure would form and the carbon walls were produced by the pyrolysis of biochar. At the same time, the carbon walls were continuously etched by KOH to create large amounts of micropores. The above discussions shed a brilliant light on the reason about the formation of 3D hierarchical porous structure of HPC<sub>2-700</sub> and why the HPPC<sub>2-700</sub> sample have not possessed 3D hierarchical porous structure. For the HPC sample, the oxygen-containing groups in the biochar were

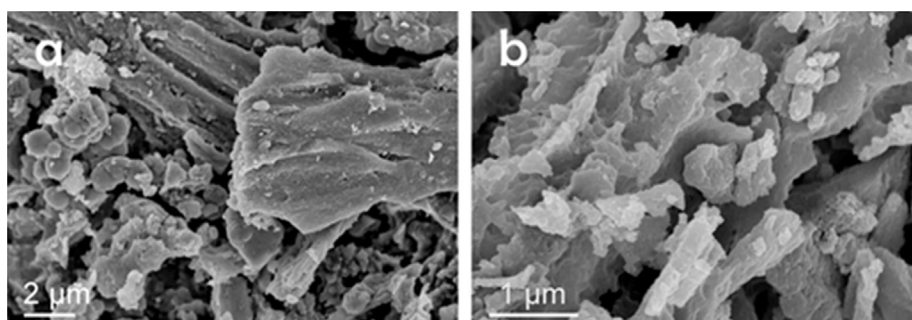


Fig. 3. SEM images of HPPC<sub>2-700</sub>.

decomposed during the pyrolysis, which made it impossible to efficiently produce molten mixture of potassium salts and biochar during the heat-treating.

Fig. 4a shows the XRD patterns of PC<sub>3-600</sub>, HPC<sub>2-700</sub> and HPPC<sub>2-700</sub>, and there are two typical peaks at about 26° and 43.3°, corresponding to the (0 0 2) and (1 0 0) plane, respectively. These weak and broad peaks indicate that these samples all belong to amorphous carbon with a low degree of graphitization. Moreover, the peak intensity of the HPPC<sub>2-700</sub> is slightly higher than HPC<sub>2-700</sub>, implying the pre-carbonization process have enhanced the degree of graphitization. The Raman spectra of PC<sub>3-600</sub>, HPC<sub>2-700</sub> and HPPC<sub>2-700</sub> are shown in Fig. 4b, and the peaks

at 1357 cm<sup>-1</sup> and 1587 cm<sup>-1</sup> correspond to D band (characteristic of disordered carbon or defective graphitic structures) and G band (characteristic feature of graphitic carbon), respectively. The intensity ratio ( $I_D/I_G$ ) of D and G bands for HPPC<sub>2-700</sub> (0.86) and HPC<sub>2-700</sub> (0.85) is higher than that of PC<sub>3-600</sub> (0.82), this shows that HPPC<sub>2-700</sub> and HPC<sub>2-700</sub> contain more defects than PC<sub>3-600</sub> due to the high content of heteroatoms (Table 1).

The porous structure of the as-obtained porous carbons was investigated using N<sub>2</sub> adsorption and desorption measurements. The N<sub>2</sub> adsorption-desorption isotherms and pore size distribution curves for all the samples are shown in Fig. 5. The N<sub>2</sub> adsorption-desorption isotherm of the PC<sub>3-600</sub> sample is typical

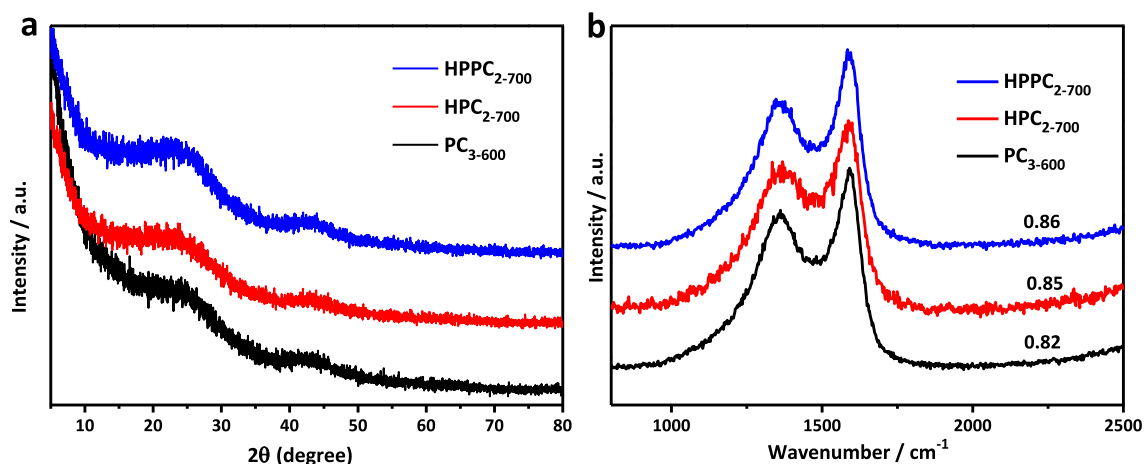


Fig. 4. (a) XRD patterns and (b) Raman spectra of the PC<sub>3-600</sub>, HPC<sub>2-700</sub> and HPPC<sub>2-700</sub>.

Table 1

The specific surface area, heteroatoms content and specific capacitance of samples.

Samples	Specific surface area (m <sup>2</sup> g <sup>-1</sup> )		Heteroatoms content (%) <sup>c</sup>		Specific capacitance <sup>d</sup> (F g <sup>-1</sup> )
	BET <sup>a</sup>	Micropore <sup>b</sup>	O	N	
PC <sub>3-600</sub>	2131	1773	8.24	1.19	390
HPC <sub>2-700</sub>	1214	1061	11.57	0.73	353
HPPC <sub>2-700</sub>	1278	1057	11.57	1.45	304

<sup>a</sup> BET method.

<sup>b</sup> t-plot method.

<sup>c</sup> obtained from XPS.

<sup>d</sup> measured in a three-electrode system at 1 A g<sup>-1</sup>.

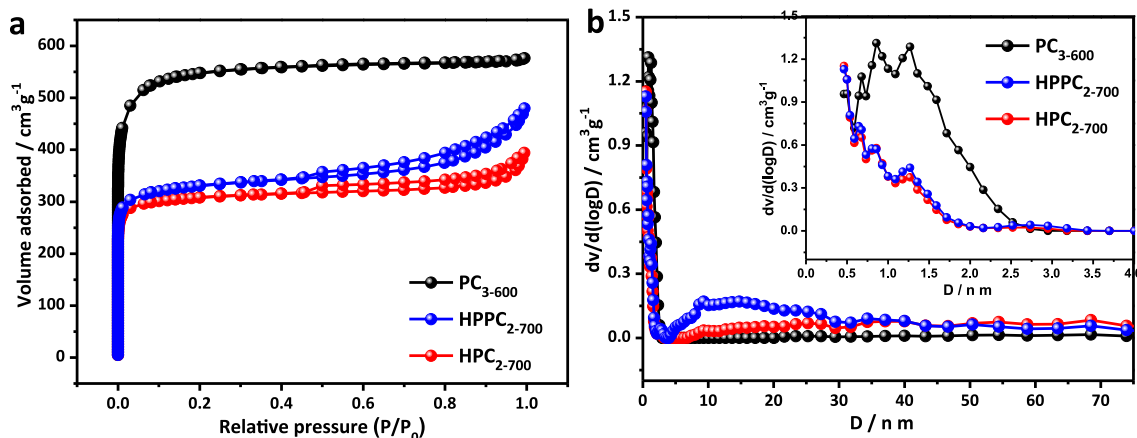


Fig. 5. (a) Nitrogen adsorption-desorption and (b) the pore size distribution curves of the PC<sub>3-600</sub>, HPC<sub>2-700</sub> and HPPC<sub>2-700</sub>.



Langmuir isotherm and belongs to the type I without hysteresis loops, indicating the presence of plentiful micropores. The curves of HPPC<sub>2-700</sub> and HPC<sub>2-700</sub> shows the rapid growth of N<sub>2</sub> adsorption in the low relative pressure area and the accretion of N<sub>2</sub> adsorption with the increase of the relative pressure accompanied by H4 hysteresis loop, which are identified as a combined Type I and IV isotherms. This result suggests that the two samples are rich in both micropore and mesopore. The pore size distribution curves (Fig. 5b) further prove that HPPC<sub>2-700</sub> and HPC<sub>2-700</sub> are rich in micropore with a small amount of mesopores, and PC<sub>3-600</sub> only contains micropores. This result is in accordance with the conclusion of N<sub>2</sub> adsorption-desorption isotherms. In addition, the specific surface area of PC<sub>3-600</sub>, HPC<sub>2-700</sub> and HPPC<sub>2-700</sub> were 2131 m<sup>2</sup> g<sup>-1</sup>, 1214 m<sup>2</sup> g<sup>-1</sup> and 1278 m<sup>2</sup> g<sup>-1</sup> with the ratio of micropore area to total specific surface area up to 83.2%, 87.4% and 82.7%, respectively (Table 1). The specific surface area of HPC<sub>2-700</sub> and HPPC<sub>2-700</sub> are lower than that of PC<sub>3-600</sub>, which is derived from the morphology change of the material during the hydrothermal process and a certain amount of mesopores formed during the activation process. PC<sub>3-600</sub> is rich in micropores and has a high specific surface area, which will be beneficial to its charge storage capability. While the certain number of mesopores existing in HPC<sub>2-700</sub> and HPPC<sub>2-700</sub> samples will help to improve rate performance.

The element composition and the information of the functional groups on the surface of the samples were obtained by X-ray photoelectron spectroscopy (XPS). Fig. 6a shows the presence of C, N, and O in the material with corresponding peaks at 283, 400, and 531 eV, respectively. The O content of PC<sub>3-600</sub> (8.24 wt%), HPC<sub>2-700</sub> (11.57 wt%) and HPPC<sub>2-700</sub> (11.57 wt%) is much higher

than the N content of which (1.19, 0.73, 1.45 wt%) (See in Table 1). The high-resolution O1s spectra of PC<sub>3-600</sub>, HPC<sub>2-700</sub> and HPPC<sub>2-700</sub> are shown in Fig. 6b–d, and found that the chemical state of oxygen in these porous carbons is different due to the difference of preparing technology. The high-resolution O1s spectrum of PC<sub>3-600</sub> samples (Fig. 6b) revealed the presence of three oxygen-based groups including carbonyl oxygen of quinones (O1, 530.87 eV), carbon-oxygen double bond (O2, 532 ± 0.1 eV) [38] and carbon-oxygen ether-like single bond and/or carbon-oxygen single-bond in hydroxyl groups (O3, 533.14 eV) [39]. The O1s spectra of HPC<sub>2-700</sub> shown in (Fig. 6c) reveals four oxygen species of O2, O3, chemisorbed oxygen (O4, 534 eV) and –COOH (O5, 535.45 eV) [40]. The oxygen species existed in HPPC<sub>2-700</sub> is similar with that in PC<sub>3-600</sub>. Comparison with HPC<sub>2-700</sub>, the –COOH in HPPC<sub>2-700</sub> has disappeared and the carbonyl oxygen of quinones has appeared due to pre-carbonation. These results indicate that the pre-carbonation has some effects on the existential state of oxygen in these porous carbon materials. The content of specific oxygen functional group is listed in Table S1. These Oxygen-containing groups can both improve wettability and provide extra reversible faradic reactions [41]. The faradic reactions probably occurred in the electrochemical testing process according to the following equations [42]:

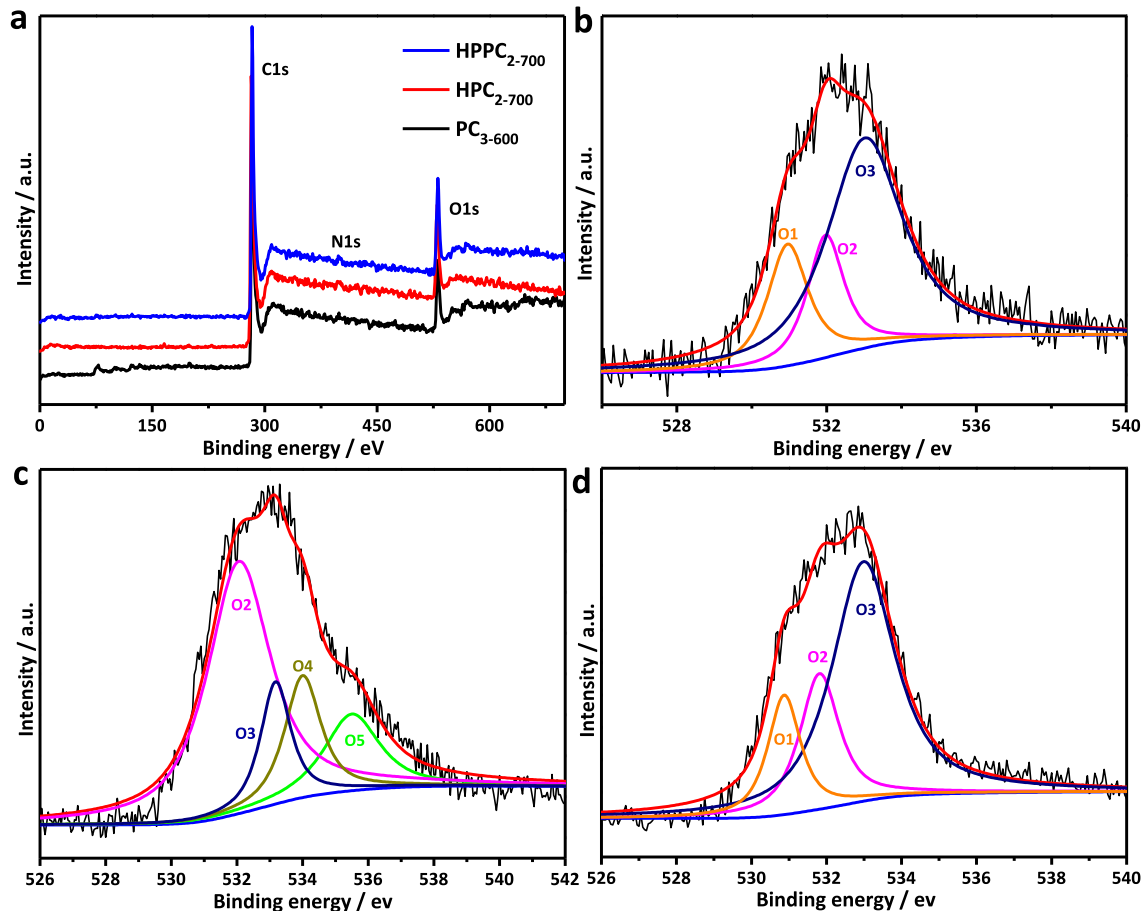
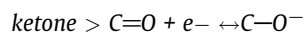
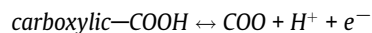
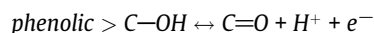


Fig. 6. (a) XPS survey spectra and (b, c, d) high resolution XPS of O 1s peaks of PC<sub>3-600</sub>, HPC<sub>2-700</sub>.

Note that, not all oxygen-containing functional groups are stable and some unstable oxygen-containing functional groups such as  $-\text{COOH}$  can lead to a reduction in the stability of the carbon electrode cycle [43].

The electrochemical properties of  $\text{PC}_{3-600}$ ,  $\text{HPC}_{2-700}$  and  $\text{HPPC}_{2-700}$  were measured in the three electrode system with 6 M KOH solution as electrolyte. The CV curves of  $\text{PC}_{3-600}$ ,  $\text{HPC}_{2-700}$  and  $\text{HPPC}_{2-700}$  (Fig. 7a) shows a nearly-rectangular shape with a wide hump in the voltage range between  $-0.8$  V and  $-0.3$  V [44], indicating that the capacitance comes from combination of double layer capacitance and pseudo-capacitive. The resembling rectangle shape proves that the samples have better capacitance characteristics and a smaller internal resistance. Other CV curves (Fig. S4) obtained at scan rates of  $10\text{--}200\text{ mV s}^{-1}$  show that the rectangular shape is only slightly distorted and still maintains a similar rectangular even at high scan rates, which demonstrates that the material has an excellent rate performance [45]. Fig. 7b compares the GCD curves of all samples, and found that the curves are close to a straight line with a little distortion, indicating that the total capacitance of these materials is mainly contribution from the double layer capacitance and a small amount of pseudo-capacitance produced by oxygen (nitrogen) group redox reactions.

The rate performance of three electrodes has further been investigated through GCD tests and the linear variation of specific capacitances at various current densities is shown in Fig. 7c. The specific capacitance of  $\text{PC}_{3-600}$ ,  $\text{HPC}_{2-700}$  and  $\text{HPPC}_{2-700}$  is as high as  $390\text{ F g}^{-1}$ ,  $353\text{ F g}^{-1}$  and  $304\text{ F g}^{-1}$  at  $1\text{ A g}^{-1}$ , respectively. And when the current density increases up to  $50\text{ A g}^{-1}$ , the specific capacitance still maintains at  $287\text{ F g}^{-1}$ ,  $270\text{ F g}^{-1}$  and  $235\text{ F g}^{-1}$  with corresponding retention ratio of 73.5%, 76.48%, 77.3%, respectively. Obviously, benefiting from the high surface area and

abundant micro-pores,  $\text{PC}_{3-600}$  displays the highest specific capacitance among them [46]. However, due to the lack of mesopores,  $\text{PC}_{3-600}$  exhibits the poorest rate performance. The  $\text{HPC}_{2-700}$  and the  $\text{HPPC}_{2-700}$  have better rate capability because the existence of mesoporous structure. By comparisons of  $\text{HPC}_{2-700}$  and  $\text{HPPC}_{2-700}$ , both of them have almost the same surface area and heteroatom content, but  $\text{HPC}_{2-700}$  displays a higher specific capacitance than  $\text{HPPC}_{2-700}$ . This indicates that the 3D frame structure is conducive to enhance effective electrochemical specific surface area for improving capacitance. The electrochemical impedance spectroscopy (EIS) of  $\text{PC}_{3-600}$ ,  $\text{HPC}_{2-700}$  and  $\text{HPPC}_{2-700}$  electrodes was analyzed in the frequency range from  $10\text{ mHz}$  to  $100\text{ kHz}$  and the results are shown in Fig. 7d. These  $\text{PC}_{3-600}$ ,  $\text{HPC}_{2-700}$  and  $\text{HPPC}_{2-700}$  electrodes show lower ohmic resistance ( $R_s$  values is  $0.65$ ,  $0.62$  and  $0.6\text{ }\Omega$ , respectively) derived from a small x-intercept. The semicircle diameter in the mediate frequency region represents the charge-transfer resistance ( $R_{ct}$ ), which is  $0.41$ ,  $0.36$  and  $0.62\text{ }\Omega$  for  $\text{PC}_{3-600}$ ,  $\text{HPC}_{2-700}$  and  $\text{HPPC}_{2-700}$  electrodes, respectively. The 3D pore structure, high content of carbon-oxygen double band and a certain amount of  $-\text{COOH}$  in  $\text{HPC}_{2-700}$  would improve the wettability and further enhance effective active area of the electrode material, leading to its smallest  $R_{ct}$  [41]. In the low-frequency region, the straight lines are almost vertical with the vertical axis, indicating their better capacitive behavior with rapid ion diffusion.

The capacitor behavior of  $\text{PC}_{3-600}$ ,  $\text{HPC}_{2-700}$  and  $\text{HPPC}_{2-700}$  was also studied with a two-electrode system. All the CV curves (Fig. 8a) for  $\text{PC}_{3-600}$ ,  $\text{HPC}_{2-700}$  and  $\text{HPPC}_{2-700}$  samples show a nearly-rectangular shape revealing their good double-layer behaviors. In addition, the CV curves of samples at higher scan rates were presented in Fig. S5 and found that the CV curve of  $\text{HPC}_{2-700}$  still

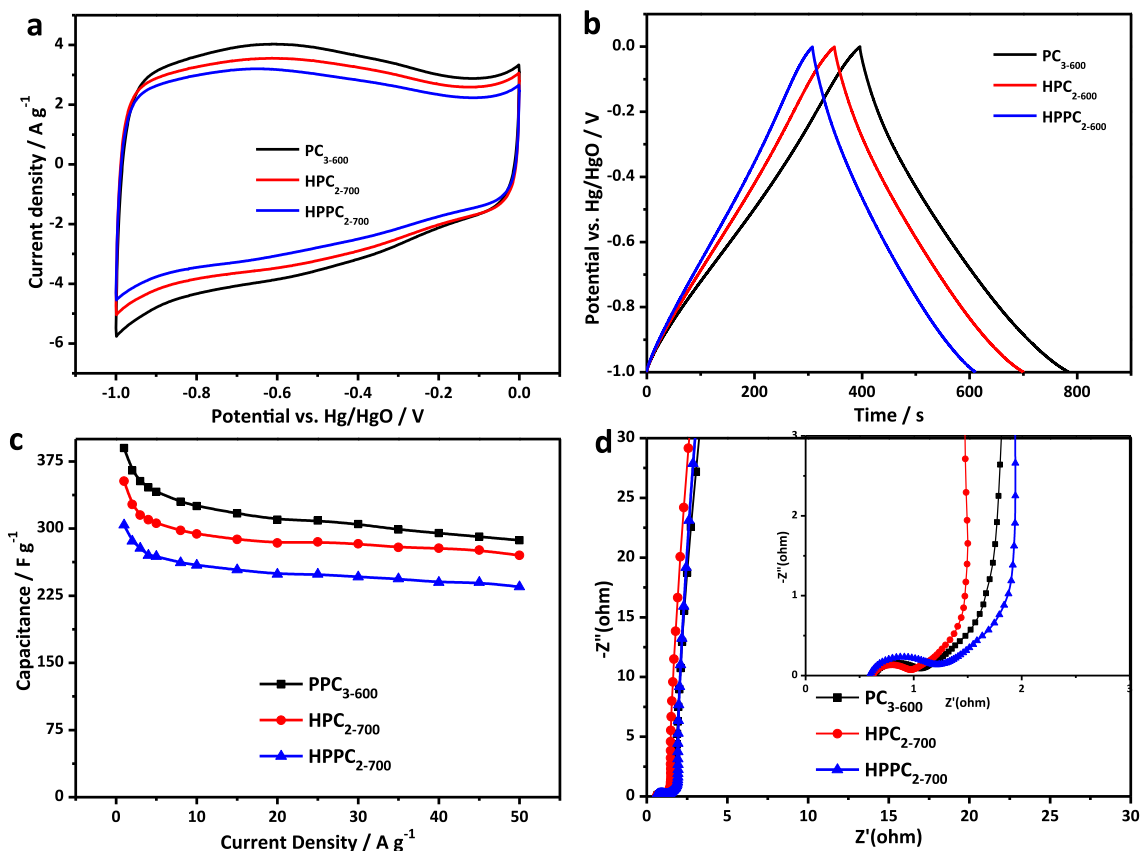


**Fig. 7.** Electrochemical performance of  $\text{PC}_{3-600}$ ,  $\text{HPC}_{2-700}$  and  $\text{HPPC}_{2-700}$  measured in a three-electrode system in the 6 M KOH electrolyte: (a) Cyclic voltammetry (CV) curves at  $10\text{ mV s}^{-1}$ ; (b) galvanostatic charge/discharge (GCD) curves at a current density of  $1\text{ A g}^{-1}$ ; (c) specific capacitances at different current densities; (d) Nyquist plots in the frequency range from  $10\text{ kHz}$  to  $10\text{ mHz}$ .



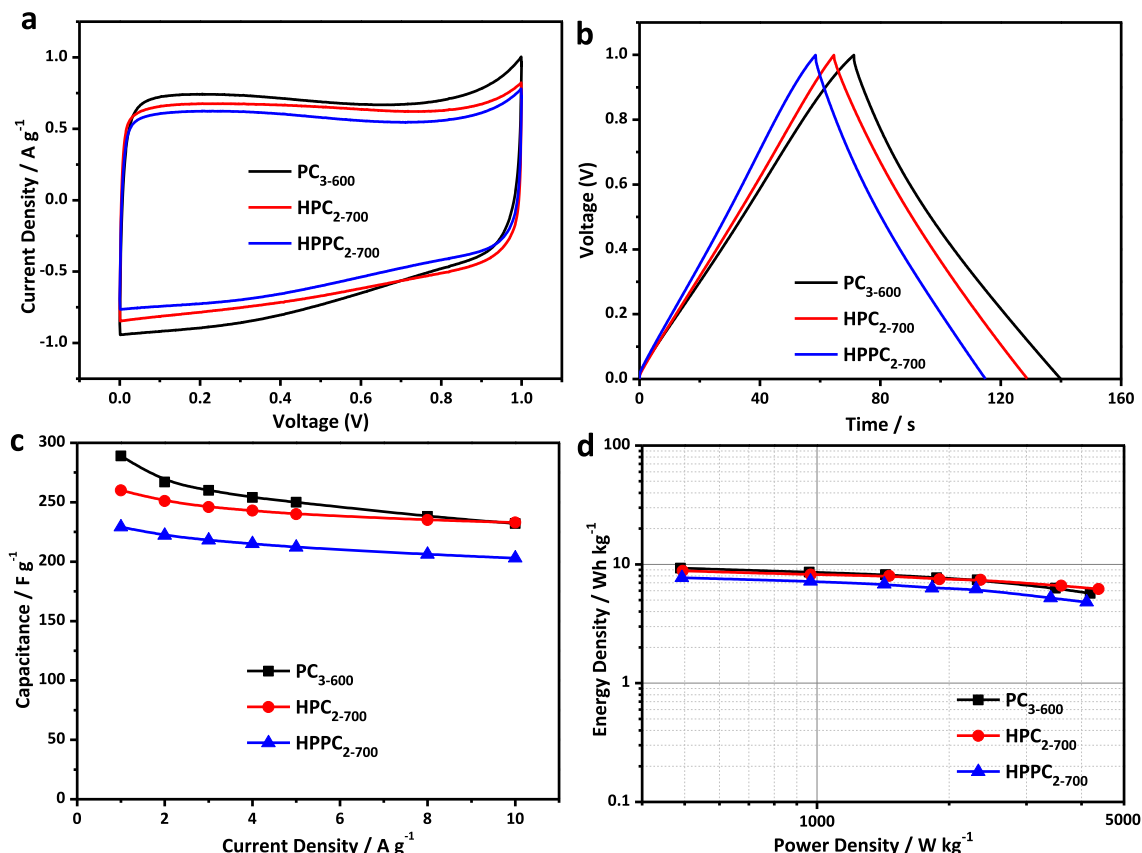


**Fig. 8.** Electrochemical performance of PC<sub>3-600</sub>, HPC<sub>2-700</sub> and HPPC<sub>2-700</sub> measured in a two-electrode system in the 6 M KOH electrolyte (a) CV curves at 10 mV s<sup>-1</sup>; (b) GCD curves at a current density of 1 A g<sup>-1</sup>; (c) specific capacitances at different current densities; (d) Ragone plot of the symmetrical system.

remains good rectangular shape at 200 mV s<sup>-1</sup> superior to other two samples, meaning that it has better rate performance. The GCD curves of all samples (Fig. 8b) show good isosceles triangle shape, suggesting that these electrodes have excellent reversible double-layer capacitive performance. The specific capacitances for these electrodes at various density currents are shown in Fig. 8c. The capacitance is 289 F g<sup>-1</sup>, 260 F g<sup>-1</sup>, 229 F g<sup>-1</sup> at 1 A g<sup>-1</sup> for PC<sub>3-600</sub>, HPC<sub>2-700</sub> and HPPC<sub>2-700</sub>, respectively. When the current density increasing up to 10 A g<sup>-1</sup>, the capacitance value maintains as high as 232 F g<sup>-1</sup>, 233 F g<sup>-1</sup> and 203 F g<sup>-1</sup> and the HPC<sub>2-700</sub> displays the highest retention ratio of 89.6% compared with other two electrodes (80.2% for PC<sub>3-600</sub>, 88.6% for HPPC<sub>2-700</sub>). This further reflects the advantages of hierarchical pore structure and a large number of oxygen-containing groups to optimize ion transport and improve the surface wettability. PC<sub>3-600</sub> delivers a high energy density of 9.3 Wh kg<sup>-1</sup> at the power density of 489 W kg<sup>-1</sup>, superior to HPC<sub>2-700</sub> and HPPC<sub>2-700</sub> with the energy density of 8.8 Wh kg<sup>-1</sup> at 495 W kg<sup>-1</sup> and 7.7 Wh kg<sup>-1</sup> at 493 W kg<sup>-1</sup> (Fig. 8d). However, HPC<sub>2-700</sub> exists the highest energy density of 6.2 Wh kg<sup>-1</sup> and power density of 4376 W kg<sup>-1</sup>, significantly higher than that of PC<sub>3-600</sub> (5.7 Wh kg<sup>-1</sup> at 4188 W kg<sup>-1</sup>) and HPPC<sub>2-700</sub> (4.8 Wh kg<sup>-1</sup> at 4114 W kg<sup>-1</sup>) at the same testing current density. This can be ascribed to the highest effective voltage of HPC<sub>2-700</sub>. From Fig. S6a (the voltage drops versus current), it can be seen that the HPC<sub>2-700</sub> has the smallest slope (3.35 Ω), indicating its smallest overall internal resistance, which could insure it having a higher effective working voltage. Cyclic stability of HPC<sub>2-700</sub> in a two-electrode system shows in Fig. S5d and found that the capacitor still retains 85.59% of its initial capacitance after 5000 cycles at 5 A g<sup>-1</sup>. The decrease in capacitance is mainly due to the deactivation of heteroatoms such as nitrogen and oxygen during charge/discharges [47,48].

According to energy density equation, the energy density of a supercapacitor is proportional to the square of the voltage range. Thus, the increase of working voltage can largely enhance the energy density of the supercapacitor. The operating voltage of supercapacitors using KOH solution as electrolyte can only reach approximately 1 V. Na<sub>2</sub>SO<sub>4</sub> electrolyte, as a neutral electrolyte, possesses a higher operation voltage of 1.6–1.8 V [49]. Therefore, Na<sub>2</sub>SO<sub>4</sub> electrolyte was used instead of KOH electrolyte to further investigate supercapacitor performance. The CV curves (Fig. 9a) and GCD curves (Fig. 9b) for a wide voltage range of 0–1.8 V indicates that these electrodes have a good double layer capacitance characteristics. The ohmic drop was calculated from the GCD curves and the curve of which changing with current is shown in Fig. S6b. The internal resistance (namely the slope of the straight line) of HPC<sub>2-700</sub> is much smaller (16.32 Ω) than that of PC<sub>3-600</sub> (23.86 Ω), and these values are substantially higher than that in KOH electrolyte (Fig. S6a) due to the low conductivity of the Na<sub>2</sub>SO<sub>4</sub> electrolyte [50]. The specific capacitance value for HPC<sub>2-700</sub> (193 F g<sup>-1</sup>) is higher than that for PC<sub>3-600</sub> (187 F g<sup>-1</sup>) at low current density of 1 A g<sup>-1</sup>. Yet, at a high current density of 10 A g<sup>-1</sup>, the specific capacitance of HPC<sub>2-700</sub> (144 F g<sup>-1</sup>) has become much higher than that of PC<sub>3-600</sub> (100 F g<sup>-1</sup>). The rate performance of HPC<sub>2-700</sub> is significantly higher than PC<sub>3-600</sub> (Fig. 9c) with respectively capacitance retention ratio of 74.61% and 53.47%. PC<sub>3-600</sub> and HPC<sub>2-700</sub> exhibit the energy density of 19.5 Wh kg<sup>-1</sup> at 862 W kg<sup>-1</sup> and 20.4 Wh kg<sup>-1</sup> at 872 W kg<sup>-1</sup> (Fig. 9d), which are more than doubled at similar power density compared with that in KOH electrolyte (8.6 Wh kg<sup>-1</sup> at 960 W kg<sup>-1</sup> and 8.2 Wh kg<sup>-1</sup> at 968 W kg<sup>-1</sup>). At large power density, then energy density of HPC<sub>2-700</sub> is 7.8 Wh kg<sup>-1</sup> at 6240 W kg<sup>-1</sup>, which is far higher than that of PC<sub>3-600</sub> (3.5 Wh kg<sup>-1</sup> at 5040 W kg<sup>-1</sup>). The energy density

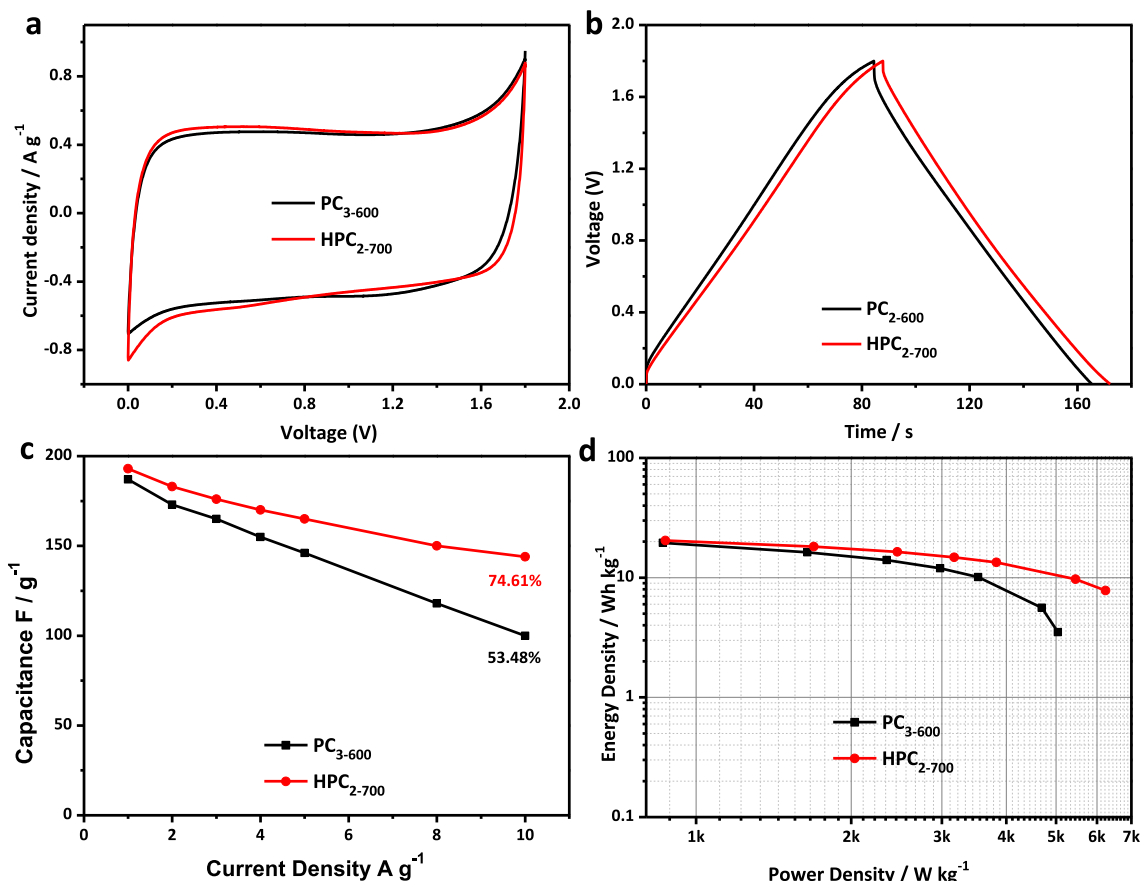


**Fig. 9.** Electrochemical performance of PC<sub>3-600</sub>, HPC<sub>2-700</sub> measured in a two-electrode system in the 1 M Na<sub>2</sub>SO<sub>4</sub> electrolyte (a) CV curves at 10 mV s<sup>-1</sup> (b) GCD curves at a current density of 1 A g<sup>-1</sup> (c) specific capacitances at different current densities (d) Ragone plot of the symmetrical system.

and power density loss of PC<sub>3-600</sub> is even more serious, because the internal resistance of the PC<sub>3-600</sub> is much higher than that of the HPC<sub>2-700</sub> resulting in the much smaller effective operating voltage. These results well reveal that the 3D frame structure with hierarchical pores is much superior to microporous structure for achieving high supercapacitor performance.

#### 4. Conclusions

In summary, mung bean husks, as biomass wastes, were explored as a sustainable carbon resource to prepare various porous carbons through multiple strategies, including direct pyrolysis activation and first hydrothermal treatment then activation. The preparation processing plays a great influence on the morphology and porous structure of those carbon materials. Especially, the formation mechanism of 3D hierarchical pore structure for HPC<sub>2-700</sub> sample has been discussed in detail. The oxygen-containing functional groups in the biochar act an important role in fabricating the 3D honeycomb-like porous structure. The HPC<sub>2-700</sub> electrode exhibits a high specific capacitance of 353 F g<sup>-1</sup> at a current density of 1 A g<sup>-1</sup> in a three electrode system. Furthermore, a high energy density of 20.4 Wh kg<sup>-1</sup> was reached at 872 W kg<sup>-1</sup> for HPC<sub>2-700</sub>//HPC<sub>2-700</sub> symmetric supercapacitor in 1 M Na<sub>2</sub>SO<sub>4</sub> electrolyte.

#### Acknowledgements

This work was supported by National Natural Science Foundation of China (21406056), Natural Science Foundation of Heilongjiang Province of China (B2017011) and Scientific Research Foundation for Post Doctor (LBH-Q17147).

#### Appendix A. Supplementary material

Additional characterization and performance results. Supplementary data to this article can be found online at <https://doi.org/10.1016/j.jcis.2018.09.055>.

#### References

- [1] X. Pu, M. Liu, L. Li, S. Han, X. Li, C. Jiang, C. Du, J. Luo, W. Hu, Z. Wang, Wearable textile-based in-plane microsupercapacitors, *Adv. Energy Mater.* 6 (2016) 1601254.
- [2] M. He, J. Ge, Z. Lin, X. Feng, X. Wang, H. Lu, Y. Yang, F. Qiu, Thermo power enhancement in conducting polymer nanocomposites via carrier energy scattering at the organic-inorganic semiconductor interface, *Energy Environ. Sci.* 5 (2012) 8351–8358.
- [3] C. Chen, D. Yu, G. Zhao, B. Du, W. Tang, L. Sun, Y. Sun, F. Besenbacher, M. Yu, Three-dimensional scaffolding framework of porous carbon nanosheets derived from plant wastes for high-performance, supercapacitors, *Nano Energy* 27 (2016) 377–389.
- [4] X. Wang, B. Liu, Q. Wang, W. Song, X. Hou, D. Chen, Y. Cheng, G. Shen, Three-dimensional hierarchical GeSe<sub>2</sub> nanostructures for high performance flexible all-solid-state supercapacitors, *Adv. Mater.* 25 (2013) 1479–1486.
- [5] L. Wang, J. Yu, X. Dong, X. Li, Y. Xie, S. Chen, P. Li, H. Hou, Y. Song, Three-dimensional macroporous carbon/Fe<sub>3</sub>O<sub>4</sub>-doped porous carbon nanorods for high-performance supercapacitor, *ACS Sustain. Chem. Eng.* 4 (2016) 1531–1537.
- [6] V. Augustyn, P. Simon, B. Dunn, Pseudocapacitive oxide materials for high-rate electrochemical energy storage, *Energy Environ. Sci.* 7 (2014) 1597–1614.
- [7] G. Wang, L. Zhang, J. Zhang, A review of electrode materials for electrochemical supercapacitors, *Chem. Soc. Rev.* 41 (2012) 797–828.
- [8] H. Jiang, P.S. Lee, C. Li, 3D carbon based nanostructures for advanced supercapacitors, *Energy Environ. Sci.* 6 (2013) 41–53.
- [9] M. Inagaki, M. Toyoda, Y. Sonea, S. Tsujimura, T. Morishita, Templated mesoporous carbons: synthesis and applications, *Carbon* 107 (2016) 448–473.
- [10] S. Wang, R. Liu, C. Han, J. Wang, M. Li, J. Yao, H. Li, Y. Wang, A novel strategy to synthesize hierarchical, porous carbohydrate-derived carbon with tunable properties, *Nanoscale* 6 (2014) 13510–13517.

- [11] J.R. Dodson, V.L. Budarin, A.J. Hunt, P.S. Shuttleworth, J.H. Clark, Shaped mesoporous materials from fresh macroalgae, *J. Mater. Chem. A* 1 (2013) 5203–5207.
- [12] Y. Li, Y.S. Hu, M.M. Titirici, L. Chen, X. Huang, Hard carbon microtubes made from renewable cotton as high-performance anode material for sodium-ion batteries, *Adv. Energy Mater.* 6 (2016) 1600659.
- [13] W.H. Qu, Y.Y. Xu, A.H. Lu, X.Q. Zhang, W.C. Li, Converting biowaste corncob residue into high value added porous carbon for supercapacitor electrodes, *Bioresour. Technol.* 189 (2015) 285–291.
- [14] J. Pu, C. Li, L. Tang, T. Li, L. Ling, K. Zhang, Y. Xu, Q. Li, Y. Yao, Impregnation assisted synthesis of 3D nitrogen-doped porous carbon with high capacitance, *Carbon* 94 (2015) 650–660.
- [15] G. Sun, B. Li, J. Ran, X. Shen, H. Tong, Three-dimensional hierarchical porous carbon/graphene composites derived from graphene oxide-chitosan hydrogels for high performance supercapacitors, *Electrochim. Acta* 171 (2015) 13–22.
- [16] L. Zhang, T. You, T. Zhou, X. Zhou, F. Xu, Interconnected hierarchical porous carbon from lignin-derived byproducts of bioethanol production for ultra-high performance supercapacitors, *ACS Appl. Mater. Interf.* 8 (2016) 13918–13925.
- [17] C. Wang, D. Wu, H. Wang, Z. Gao, F. Xu, K. Jiang, A green and scalable route to yield porous carbon sheets from biomass for supercapacitors with high capacity, *J. Mater. Chem. A* 6 (2018) 1244–1254.
- [18] Z. Li, Z. Xu, H. Wang, J. Ding, B. Zahir, C.M.B. Holt, X. Tan, D. Mitlin, Colossal pseudo-capacitance in a high functionality–high surface area carbon anode doubles the energy of an asymmetric super-capacitor, *Energy Environ. Sci.* 7 (2014) 1708–1718.
- [19] T. Guan, K. Li, J. Zhao, R. Zhao, G. Zhang, D. Zhang, J. Wang, Template-free preparation of layer-stacked hierarchical porous carbons from coal tar pitch for high performance all-solid-state supercapacitors, *J. Mater. Chem. A* 5 (2017) 15869–15878.
- [20] J.W. Lee, H.I. Lee, S.J. Park, Facile synthesis of petroleum-based activated carbons/tubular polypyrrole composites with enhanced electrochemical performance as supercapacitor electrode materials, *Electrochim. Acta* 263 (2018) 447–453.
- [21] S.T. Senthilkumar, R.K. Selvan, Flexible fiber supercapacitor using biowaste-derived porous carbon, *ChemElectroChem* 2 (2015) 1111–1116.
- [22] M. Genovese, J. Jiang, K. Lian, N. Holm, High capacitive performance of exfoliated biochar nanosheets from biomass waste corn cob, *J. Mater. Chem. A* 3 (2015) 2903–2913.
- [23] L. Wang, Y. Zheng, Q. Zhang, L. Zuo, S. Chen, S. Chen, H. Hou, Y. Song, Template-free synthesis of hierarchical porous carbon derived from low-cost biomass for high performance supercapacitors, *RSC Adv.* 4 (2014) 51072–51079.
- [24] D. Ma, G. Wu, J. Wan, F. Ma, W. Geng, S. Song, Oxygen-enriched hierarchical porous carbon derived from biowaste sunflower heads for high performance supercapacitors, *RSC Adv.* 5 (2015) 107785–107792.
- [25] T. Kan, V. Strezov, T.J. Evans, Lignocellulosic biomass pyrolysis: a review of product properties and effects of pyrolysis parameters, *Renew. Sustain. Energy Rev.* 57 (2016) 1126–1140.
- [26] Z. Qiu, Y. Wang, X. Bi, T. Zhou, J. Zhou, J. Zhao, Z. Miao, W. Yi, P. Fu, S. Zhuo, Biochar-based carbons with hierarchical micro-meso-macro porosity for high rate and long cycle life supercapacitors, *J. Power Source.* 376 (2018) 82–90.
- [27] Q. Wang, L. Ma, K. Jiao, Q. Zhang, Y. Kou, J. Xu, W. Cao, Optimization extraction of insoluble dietary fiber from phaseolus radiatus hull and its properties, *Farm Prod. Process.* 7 (2015) 12–15 ([www.cnki.net](http://www.cnki.net)).
- [28] K. Zhong, W. Lin, Q. Wang, S. Zhou, Extraction and radicals scavenging activity of polysaccharides with microwave extraction from mung bean hulls, *Int. J. Biol. Macromol.* 51 (2012) 612–617.
- [29] F. Lai, Q. Wen, L. Li, H. Wu, X. Li, Antioxidant activities of water-soluble polysaccharide extracted from mung bean (*Vigna radiata* L.) hull with ultrasonic assisted treatment, *Carbohydr. Polym.* 81 (2010) 323–329.
- [30] S. Mondal, K. Sinha, K. Aikat, G. Halder, Adsorption thermodynamics and kinetics of ranitidine hydrochloride onto superheated steam activated carbon derived from mung bean husk, *J. Environ. Chem. Eng.* 3 (2015) 187–195.
- [31] S.T. Senthilkumar, R.K. Selvan, J.S. Melo, C. Sanjeeviraja, High performance solid-state electric double layer capacitor from redox mediated gel polymer electrolyte and renewable tamarind fruit shell derived porous carbon, *ACS Appl. Mater. Interf.* 5 (2013) 10541–10550.
- [32] J. Wang, Q. Liu, Fungi-derived hierarchically porous carbons for high-performance supercapacitors, *RSC Adv.* 5 (2015) 4396–4403.
- [33] P. Kumar, D.M. Barrett, M.J. Delwiche, P. Stroeve, Methods for pretreatment of lignocellulosic biomass for efficient hydrolysis and biofuel production, *Ind. Eng. Chem. Res.* 48 (2009) 3713–3729.
- [34] M. Sevilla, A.B. Fuertes, R. Mokaya, High density hydrogen storage in superactivated carbons from hydrothermally carbonized renewable organic materials, *Energy Environ. Sci.* 4 (2011) 1400–1410.
- [35] S. Song, F. Ma, G. Wu, D. Ma, W. Geng, J. Wan, Facile self-templating large scale preparation of biomass-derived 3D hierarchical porous carbon for advanced supercapacitors, *J. Mater. Chem. A* 3 (2015) 18154–18162.
- [36] M.M. Titirici, M. Antonietti, Chemistry and materials options of sustainable carbon materials made by hydrothermal carbonization, *Chem. Soc. Rev.* 39 (2010) 103–116.
- [37] J. Deng, T. Xiong, F. Xu, M. Li, C. Han, Y. Gong, H. Wang, Y. Wang, Inspired by bread leavening: one-pot synthesis of hierarchically porous carbon for supercapacitors, *Green Chem.* 17 (2015) 4053–4060.
- [38] J. Shao, F. Ma, G. Wu, W. Geng, S. Song, J. Wan, D. Ma, Facile preparation of 3D nanostructured O/N co-doped porous carbon constructed by interconnected carbon nanosheets for excellent-performance supercapacitors, *Electrochim. Acta* 222 (2016) 793–805.
- [39] J. Ding, H. Wang, Z. Li, K. Cui, D. Karpuzov, X. Tan, A. Kohandehghan, D. Mitlin, Peanut shell hybrid sodium ion capacitor with extreme energy–power rivals lithium ion capacitors, *Energy Environ. Sci.* 8 (2015) 941–955.
- [40] Q. Li, L. Dong, Y. Liu, H. Xie, C. Xiong, A carbon black derivative with liquid behavior, *Carbon* 49 (2011) 1047–1051.
- [41] F. Ma, J. Wan, G. Wu, H. Zhao, Highly porous carbon microflakes derived from catkins for high-performance supercapacitors, *RSC Adv.* 5 (2015) 44416–44422.
- [42] W. Zhang, H. Lin, Z. Lin, J. Yin, H. Lu, D. Liu, M. Zhao, 3D hierarchical porous carbon for supercapacitors prepared from lignin through a facile template-free method, *ChemSusChem* 8 (2015) 2114–2122.
- [43] C. Wang, Y. Zhou, L. Sun, P. Wan, X. Zhang, J. Qiu, Sustainable synthesis of phosphorus- and nitrogen-co-doped porous carbons with tunable surface properties for supercapacitors, *J. Power Source.* 239 (2013) 81–88.
- [44] Q. Liang, L. Ye, Z. Huang, Q. Xu, Y. Bai, F. Kang, Q. Yang, A honeycomb-like porous carbon derived from pomelo peel for use in high-performance supercapacitors, *Nanoscale* 6 (2014) 13831–13837.
- [45] X. Fan, C. Yu, J. Yang, Z. Ling, C. Hu, M. Zhang, J. Qiu, A layered- nanospace-confinement strategy for the synthesis of two-dimensional porous carbon nanosheets for high-rate performance supercapacitors, *Adv. Energy Mater.* 5 (2014) 1401761.
- [46] P. Yu, Z. Zhang, L. Zheng, F. Teng, L. Hu, X. Fang, A novel sustainable flour derived hierarchical nitrogen-doped porous carbon/polyaniline electrode for advanced asymmetric supercapacitors, *Adv. Energy Mater.* 6 (2016) 1601111.
- [47] M.J. Bleda-Martínez, J.A. Maciá-Agulló, D. Lozano-Castelló, E. Morallón, D. Cazorla-Amorós, A. Linares-Solano, Role of surface chemistry on electric double layer capacitance of carbon materials, *Carbon* 43 (2005) 2677–2684.
- [48] V. Ruiz, C. Blanco, E. Raymundo-Piñero, V. Khomenko, F. Béguin, R. Santamaría, Effects of thermal treatment of activated carbon on the electrochemical behaviour in supercapacitors, *Electrochim. Acta* 52 (2007) 4969–4973.
- [49] C. Zhong, Y. Deng, W. Hu, J. Qiao, L. Zhang, J. Zhang, A review of electrolyte materials and compositions for electrochemical supercapacitors, *Chem. Soc. Rev.* 44 (2015) 7484–7539.
- [50] J. Shao, F. Ma, G. Wu, C. Dai, W. Geng, S. Song, J. Wan, In-situ MgO (CaCO<sub>3</sub>) templating coupled with KOH activation strategy for high yield preparation of various porous carbons as supercapacitor electrode materials, *Chem. Eng. J.* 321 (2017) 301–313.